Published in final edited form as:
Invest Radiol. 2011 February ; 46(2): 132–140. doi:10.1097/RLI.0b013e3181f8e7d8.

Theranostics with Multifunctional Magnetic Gold Nanoshells: Photothermal Therapy and T2* Magnetic Resonance Imaging

Marites P. Melancon, PhD[*,†], **Andrew Elliott, PhD**[†], **Xiaojun Ji, PhD**[*], **Anil Shetty, MBBS**[†], **Zhi Yang, PhD**[*], **Mei Tian, MD**[*], **Brian Taylor, PhD**[†], **R. Jason Stafford, PhD**[†], and **Chun Li, PhD**[*,*]

[*]Department of Experimental Diagnostic Imaging The University of Texas M. D. Anderson Cancer Center, Houston, TX

[†]Department of Imaging Physics, The University of Texas M. D. Anderson Cancer Center, Houston, TX

Abstract

Objectives—To investigate the multifunctional imaging and therapeutic capabilities of core-shell nanoparticles composed of a superparamagnetic iron oxide (SPIO) core and a gold shell (SPIO@AuNS).

Materials and Methods—The magnetic/optical properties of SPIO@AuNS were examined both in an agar gel phantom and *in vivo* by evaluating contrast-enhanced MRI and by measuring near-infrared (NIR) light-induced temperature changes mediated by SPIO@AuNS. In addition, the biodistribution and pharmacokinetics of ^{111}In-labeled SPIO@AuNS after intravenous injection in mice bearing A431 tumors were evaluated in the presence and absence of an external magnet.

Results—In agar phantoms containing SPIO@AuNS, a significant contrast enhancement in T2-weighted MRI was observed and a linear increase in temperature was observed with increasing concentration and laser output power when irradiated with NIR light centered at an 808-nm. *In vivo*, T_2*-MRI delineated SPIO@AuNS and magnetic resonance temperature imaging of the same tumors revealed significant temperature elevations when intratumorally injected with SPIO@AuNS (1×10^{11} particles/mouse) and irradiated with NIR light (65.70 ± 0.69°C vs. 44.23 ± 0.24°C for saline + laser). Biodistribution studies in mice intravenously injected with ^{111}In-labeled-SPIO@AuNS(1×10^{13} particles/mouse) had an approximately 2-fold increase in SPIO@AuNS delivered into tumors in the presence of an external magnet compared to tumors without the magnet.

Conclusions—Owing to its ability to mediate efficient photothermal ablation of cancer cells under MRI guidance, as well as the ability to be directed to solid tumors with an external magnetic field gradient, multifunctional SPIO@AuNS is a promising theranostic nano-platform.

Keywords

theranostics; gold nanoshells; T_2* magnetic resonance imaging; photothermal ablation; ultrasmall paramagnetic iron oxide

[*]**Address correspondence to:** Chun Li, PhD, Department of Experimental Diagnostic Imaging, The University of Texas M. D. Anderson Cancer Center, Unit 059, 1515 Holcombe Boulevard, Houston, TX 77030. Phone: 713-792-5182; Fax: 713-794-5456; cli@mdanderson.org.
Z.Y. is on leave from the Department of Nuclear Medicine, Peking University School of Oncology and Beijing Cancer Hospital, Beijing, People's Republic of China, 100036.

INTRODUCTION

The role of thermal ablation in the management of cancer has gained increasing attention over the past decade. Thermal ablation is the use of heat to directly destroy tissue. Many different energy sources have been used for thermal ablation, including radiofrequency, high-intensity focused ultrasonography, microwave, alternating magnetic field, and laser [1–8]. Heating energy can be applied by external means or by internal means via interstitial, intraluminal, or intracavitary approaches [9]. Laser-induced photothermal ablation (PTA) has been used successfully for the ablation of tumors throughout the body, especially liver lesions [2, 5]. However, because of the heat-sink effect, which dissipates heat and reduced the potency of the thermal effect, it is difficult to effectively treat lesions near large vascular structure using laser ablation alone [10].

To improve the efficacy and selectivity of laser-induced PTA, it is necessary to introduce light-absorbing materials into the tumor to mediate the photothermal effect. Gold nanoshells (AuNS), composed of metallic gold and a dielectric core, such as silica or water, are strong near-infrared (NIR) absorbers and, therefore, effective photothermal coupling agents [11–14]. Absorbance of NIR light is desirable because NIR light itself causes minimal thermal injury and optimally penetrates normal tissues [15, 16]. Successful ablation of tumor cells has been demonstrated both *in vitro* and *in vivo* using various gold nanostructures and targeting scheme [11, 13, 14, 17, 18].

The successful translation of PTA into the clinic will require 1) the ability to perform the PTA procedure under image guidance so that laser energy can be directly deposited in the target volume with accurate spatial control, 2) ability to predict heat-induced tumor cell death on the basis of intratumoral distribution of the photothermal coupling agents using appropriate thermal dosimetry model, 3) noninvasive real-time monitoring of the heat profile and response to therapy in a given target volume, and 4) selective delivery of a sufficient amount of AuNS to tumor tissue to mediate a photothermal effect. MRI is a suitable imaging modality for guiding PTA because of its high temporal and spatial resolution. Moreover, progress in magnetic resonance temperature imaging (MRTI) has opened the door to noninvasive assessment of surgical textile implants [19], local recurrence of prostate cancer after external beam radiation therapy [20], and thermal damage [21]. Several MR parameters are temperature sensitive, including the relaxation times (T_1 and T_2), bulk magnetization, and the proton resonance frequency. The latter has been shown to be most sensitive to temperature and is most commonly used to monitor temperature change during thermal ablation, with temperature errors limited to 0.5°C to 1°C [22, 23]. Our previous work has validated MRTI in large animals [24] and in a small animal model using human tumor xenografts [12].

The goal of this study was to demonstrate both in a phantom and *in vivo*, that multifunctional MRI-visible AuNS, which combine both imaging and therapeutic capabilities, is suitable for PTA therapy under MRI guidance. In addition, we evaluated whether these magnetic core-shell gold nanoparticles could be selectively directed to tumors using an external magnetic field gradient, as was done using superparamagnetic iron oxide (SPIO) nanoparticles [25, 26].

MATERIALS AND METHODS

An outline of the experiments performed is shown in Schema 1. The detailed procedure for each of the experiments listed is discussed below.

Synthesis and characterization of SPIO@AuNS

SPIO@AuNS was synthesized using methods described by Ji et al. [27]. Briefly, SPIO nanoparticles of about 10 nm in diameter (EMG 304, Ferrotech, Nashua, NH) were coated with amorphous silica via the sol-gel process. Next, gold nanocrystal seeds (2–3 nm) were introduced onto an amine-functionalized silica surface and used to nucleate the growth of a gold overlayer to form a gold nanoshell. Thiolated poly(ethylene) glycol (PEG-SH) was attached to the surface of the SPIO@AuNS by adding 5 μM of PEG-SH (final concentration) to 1×10^{12} particles/mL nanoshell in deionized water. After 2 hours, the solution was centrifuged for 5 min at 8,000 RPM and washed thrice with deionized water. The resulting solution was resuspended in 0.1 M phosphate-buffered saline (PBS).

The average diameter of the synthesized SPIO@AuNS was measured by transmission electron microscope (TEM; JEOL 2010, JEOL Ltd., Tokyo, Japan) at an accelerating voltage of 80 kV. For sample analysis, a drop of the sample solution was placed on a 400-mesh copper grid until dried. The absorption of the SPIO@AuNS was determined using an ultraviolet-vis absorption spectrophotometer (DU-800, Beckman Coutler, Fullerton, CA).

Rapid chemical shift imaging for T2* mapping and MR temperature imaging

Imaging studies were performed in a 1.5-T clinical MR scanner (Excite HD, GEHT, Waukesha, WI). A multiple, fast-gradient, refocused echo (MFGRE) was used, with 16 echoes at echo times ranging from 2 to 60 ms for each repetition time (TR). T2* maps were calculated using the Steiglitz-McBride algorithm, which has recently been shown to provide accurate and precise T2* estimates, even in the presence of lipid [28, 29]. This technique also calculates the proton resonant frequency to estimate temperature changes, thereby providing simultaneous T2* mapping and MRTI.

Magnetic and optical properties of SPIO@AuNS in agar phantoms

To determine the behavior of SPIO@AuNS in agar phantoms, 6.7×10^{11} NS/mL SPIO@AuNS was embedded in agar gel. This was done by adding 1.5 g of agar to 100 mL of deionized water. The solution was stirred with heating at 80°C until a clear solution was obtained. Then, 6.7×10^{11} NS/mL SPIO@AuNS was added to the agar solution and allowed to solidify for a few hours at 4°C. After the agar gel containing SPIO@AuNS hardened, agar gel with saline was added on top, and the gel was allowed to re-form for another 1 hr. After the MR imaging, the same gel was irradiated with an 808-nm NIR laser (continuous wave GCSLX-05-1600 m-1 fiber-coupled diode laser, DHC, China Daheng Group, Inc., Beijing, China) for 150 sec at 24 W/cm^2. The temperature was monitored 30 s before the laser was turned on, during laser irradiation (150 s), and for 3 min after laser treatment (total time = 360 s) using MRTI technique.

To study the effect of nanoshell concentration on temperature elevation, different nanoshell concentrations, ranging from 1×10^{11} to 7×10^{11} particles/mL, were embedded in agar gels. The temperature increase was measured with complex phase-difference MRTI (TR/TE/FA = 20.7 ms/9.6 ms/30°, field of view = 9 × 5 cm, matrix size = 256 × 192, and slice thickness = 3 mm) when the gels were irradiated at a constant laser power of 6 W for 2 min. Similarly, the effect of laser output power was determined by varying the laser output power from 7 to 9 W at a constant nanoshell concentration of 6×10^{11} NS/mL.

To measure the temperature sensitivity coefficients, the agar gel containing SPIO@AuNS at a concentration of 6.7×10^{11} NS/mL was heated in a water bath and cooling was observed using MRTI via the MFGRE acquisition (TR/ minimum TE/FA = 70 ms/3.1 ms/30°, echo-spacing=3.3 ms; field of view = 9 × 5 cm, matrix size = 128 × 128, and slice thickness = 3 mm). An invasive Luxtron® fluoroptic probe (M3300, Luxtron, Santa Clara, CA) was used

for single-point temperature measurement to independently validate the MRTI data. The data obtained with the temperature probe were in agreement with those obtained with MRTI. The temperature sensitivity was calculated as the slope of the regression line for the frequency shift (Δf in ppm) versus temperature change (ΔT).

In vivo T_2* imaging and PTA therapy

Human epithelial carcinoma cell line, A431, was obtained from the American Type Culture Collection (Rockville, MD, USA). Cells were maintained at 37°C in a humidified atmosphere containing 5% CO_2 in Dulbecco's modified Eagle's medium and nutrient mixture F-12 Ham containing 10% fetal bovine serum (GIBCO, Grand Island, NY, USA).

All experiments involving animals were done in accordance with the guidelines of the Institutional Animal Care and Use Committee. A431 tumors were grown on one hind leg of each nude mouse (20–25 g; Harlan-Sprague-Dawley) by subcutaneously injecting 1×10^6 viable tumor cells suspended in PBS. When the tumors had grown to 1–1.5 cm in average diameter (~2 weeks), the mice were randomly divided into 2 groups (3 mice in each group). Power greater than 80% using 2-sample t-test analysis was used to assess the suitability of the number of subjects based on the mean maximum heating achieved and the standard deviation of the different groups.

Mice in group 1 were injected intratumorally with SPIO@AuNS (100 μL, 1×10^{12} nanoparticles/mL), and mice in group 2 were injected intratumorally with saline (100 μL). Twenty-four hours after injection, MRI was used to locate the nanoshells and monitor the temperature change during treatment. Imaging studies were performed in a 1.5-T clinical MR scanner (Excite HD, GEHT, Waukesha, WI). After anesthesia induction with isoflurane (2–4%), animals were placed on a receive-only surface coil designed specifically for imaging small animals. The MFGRE acquisition was performed with the following parameters for simultaneous T2* mapping and MRTI: TR/ minimum TE/FA = 70 ms/3.1 ms/40°, field of view = 60 × 30 mm, matrix size = 128 × 128, and slice thickness = 3 mm, 5 sec/image. Tumors were irradiated with the NIR laser (808 nm at 4 W/cm^2 for 3 min). This laser power was adapted from previously published studies [12–14]. MRTI was performed 30 s before laser treatment, during laser treatment (180 s), and 90 s after laser treatment. The change in temperature was independently monitored using the Luxtron probe at three time points: 30 s before laser treatment, during laser treatment (at 120 s), and 90 s after laser treatment. Body core temperature was measured rectally with a second thermo-optic probe.

Twenty-four hours after laser irradiation (48 hours after injection of SPIO@AuNS or saline), the mice were sacrificed and the tumors were collected. The tumors were then fixed in 10% formalin, processed, cut into 5-μm slices, stained with hematoxylin and eosin, and examined using a Leica microscope (Leica Microsystems, Bannockburn, IL). Quantification of the extent of necrosis was done by manually contouring the areas of necrosis and whole tumor using Image J software (available at http://rsb.info.nih.gov/ij; developed by Wayne Rasband, National Institutes of Health, Bethesda, MD) in H & E stained slides. The percent necrosis (% necrosis) was calculated by dividing the area of necrosis by the area of the whole tumor multiplied by 100. The difference among the groups was considered statistically significant if $p\text{-}value < 0.05$ using a two-tailed Student's *t* test.

Radiolabeling

Pharmacokinetics and biodistribution studies were performed using Indium-111 (^{111}In)-labeled SPIO@AuNS. This was synthesized by conjugating diethylenetriaminepentaacetic acid (DTPA)-thioctic acid (DTPA-TA) on the surface of SPIO@AuNS. DTPA-TA was synthesized as described by Zhang et al. [30]. PEG-SH was then added to the DTPA-TA

treated SPIO@AuNS to enhance its colloidal stability. After purification, the nanoshell was resuspended in sodium acetate buffer (pH = 5). About 500 μCi of $^{111}InCl_3$ (Iso-Tex Diagnostics, Inc., Houston, TX, USA) was then added to the conjugated nanoshells. After incubation at room temperature for 20 min, the labeled nanoshells were purified by centrifugation (5 min at 8,000 rpm). The labeling efficiency was determined by instant thin-layer chromatography (ITLC). The ITLC strips were developed with PBS (pH 7.4) containing 4 mM ethylenediaminetetraacetic acid (EDTA) and quantified using a Bioscan IAR-2000 TLC imaging scanner (Washington, DC, USA). Free $^{111}In^{3+}$ moved to the solvent front (Rf = 0.9–1.0), and the nanoparticles remained at the original spot (Rf = 0.0).

Pharmacokinetics

Seven healthy female BALB/c mice (22–25 g; Charles River Laboratories, Wilmington, MA, USA) were injected with radiolabeled SPIO@AuNS intravenously at a dose of 100 μL of 1×10^{14} particles/mL (65–80 μCi/mouse). At predetermined intervals, 10 μL of blood was taken from the tail vein, and the radioactivity of each blood sample was measured with a Cobra Autogamma counter (Packard, Downers Grove, IL, USA). The blood pharmacokinetic parameters for the radiotracer were analyzed with a two-compartmental model using WinNonlin 4.1 software (Pharsight Corp., Palo Alto, CA, USA). Animals were euthanized by CO_2 exposure 48 h after SPIO@AuNS injection.

Biodistribution

In the biodistribution studies, ten nude mice bearing A431 tumors were used. A431 cell inoculation was done as described earlier in Materials and Methods. Tumor-bearing mice were randomly allocated into 2 groups. In this study, we expect a power greater than 80% using 2-sample t-test analysis was used to assess the suitability of the number of subjects based on the mean intratumoral distribution and the standard deviation of the different groups. In group 1 mice (n = 5), a 1/4 inch diameter × 1/16 inch thick circular Nd-Fe-B magnet having a pulling force = 1.6 lbs. (Applied Magnets, Plano, TX) was taped on the surface of the skin above the tumors, while mice in group 2 served as controls (no magnets). Then, ^{111}In-labeled, PEGylated SPIO@AuNS were then injected intravenously at 50 μCi per mouse (equivalent to 1×10^{13} particles/mouse). Twenty-four hours post-injection, the magnet was removed and the mice were sacrificed. Blood, heart, liver, spleen, kidney, lung, muscle, and tumor were excised and weighed. The radioactivity of the organs and tumor was measured using a Cobra γ counter (Packard). The uptake of nanoshells in the tumors was calculated as the percent injected dose per gram of tissue (%ID/g). Comparisons between the 2 groups were calculated using Student's t test, with $p \leq 0.05$ considered to be statistically significant.

RESULTS

Synthesis and characterization of SPIO@AuNS

The synthesized SPIO@AuNS had an SPIO core with silica as an interface and gold on the surface (Fig. 1A). TEM revealed nanoparticles with an average diameter of 90 nm. The Fe_2O_3 particles, each around 12 nm in diameter, were embedded inside the silica spheres. On the surface of the silica spheres, Au nanoparticles were dispersed around it having 7 nm in diameter (Fig. 1B). Conjugation with PEG-SH resulted in nanoshells that could be readily resuspended in 0.01 M PBS. PEGylated SPIO@AuNS displayed a strong plasmon absorption at 650–900 nm (Fig. 1C).

Magnetic and optical properties of SPIO@AuNS in agar phantoms

The magnetic and optical properties of SPIO@AuNS were studied using agar phantoms. T2-weighted MRI clearly showed the darkening of the lower part of the agar gel containing SPIO@AuNS, while the top gel layer without SPIO@AuNS did not show contrast enhancement (Fig. 2A). When irradiated with an 808-nm NIR laser, the temperature in the gel containing SPIO@AuNS climbed as much as 40°C within 150 s of laser irradiation in agar gel containing SPIO@AuNS at a concentration of 6.7×10^{11}. The temperature of the gel dropped immediately after the NIR laser was turned off and within one and half minute the temperature had decreased by about 10°C above room temperature (Fig. 2B).

Figure 2C shows the effect of nanoshell concentration on temperature elevation at a constant laser power of 6 W/cm^2 for 2 min. The temperature increase was directly proportional to the increase in nanoshell concentration. Similarly, there was a linear relationship between temperature increase and laser power at a constant nanoshell concentration of 6×10^{11} NS/mL (Fig. 2D). Figures 2E & 2F show the plot of frequency shift (Δf in ppm) versus temperature change (ΔT) in agar gels with and without SPIO@AuNS. The slope of the two regression lines was identical, indicating that presence of the SPIO in SPIO@AuNS did not affect the temperature sensitivity in MRTI measurements.

In vivo T_2* imaging and PTA therapy

Figure 3 shows the T_2* map of the tumor before and after intratumoral injection of SPIO@AuNS. The darkening of the tumor in the presence of SPIO@AuNS was clearly visualized. The T_2* values decreased from a pre-injection value of 12.6 ± 2.4 ms to a post-injection value of 4.0 ± 0.5 ms. The T_2* values remained unchanged after laser irradiation (T_2* = 4.0 ± 0.5 ms).

Figure 4A shows a representative MRTI map of the tumors immediately after laser irradiation. There was a greater increase in temperature in the tumor that was injected with SPIO@AuNS than in the one that was injected with saline. There was also a greater temperature increase on the outer surface of the tumor than in the inner part of the tumor. The temperature increase was plotted as a function of time for selected treatment volumes (Fig. 4B). The temperature of the treatment volume in the tumor injected with SPIO@AuNS at a dose of 1.0×10^{12} reached 65.70 ± 0.69°C when irradiated with the NIR laser, whereas the treatment volume at approximately the same depth (~4 mm) in the tumor injected with saline reached a temperature of only 44.23 ± 0.23°C. Figure 4C shows a plot of temperature versus distance measured from the entry point along the NIR light path. The tumor injected with SPIO@AuNS consistently displayed higher temperature than the tumor injected with saline over the entire NIR light path. However, the temperature difference between the two treatment groups along the light path was gradually narrowed towards the NIR light exiting site (Fig. 4C).

Pathological results confirm that the tumors treated with SPIO@AuNS and irradiated with the NIR laser had a significantly greater degree of necrosis (% necrosis = 52.63 ± 7.85) than the tumors treated with saline (19.4 ± 9.65) and the NIR laser (16.81 ± 10.72) or the tumors treated with SPIO@AuNS alone (14.67 ± 8.99) (Fig. 5E).

Pharmacokinetics and biodistribution

To determine whether the efficiency of the delivery of SPIO@AuNS could be enhanced in the presence of an external magnetic field gradient, SPIO@AuNS was labeled with the gamma emitter ^{111}In ($t_{1/2}$ = 2.7 days) to facilitate quantitative pharmacokinetic and biodistribution studies. A disulfide metal chelator capable of providing a strong bond with

the surface of gold, DTPA-TA, was used as the metal chelator (Fig. 6A) [30]. The labeling efficiency was >99%, as determined by ITLC.

Figure 6B shows the blood activity-time profile of ^{111}In-labeled, PEGylated SPIO@AuNS. The data were fitted to a two-compartmental model using the following equation:

$$C_t\left(\%\text{ID g}^{-1}\text{ blood}\right)=A\mathrm{e}^{-\alpha t}+B\mathrm{e}^{-\beta t}$$

where A and B are the y intercepts of the extrapolated lines for the central and tissue compartments, respectively, and α and β are first-order rate constants for the central and tissue compartments, respectively. The mean pharmacokinetic equation for the ^{111}In-labeled SPIO@AuNS was

$$C_t=17.03\mathrm{e}^{-0.085t}+6.082\mathrm{e}^{-0.004t}$$

Calculation of the blood half-lives of the distribution ($T_{1/2,\alpha}$) and clearance ($T_{1/2,\beta}$) phases showed values of 10.7 ± 5.24 (min) and 163.7 ± 21.2 (min), respectively, for PEGylated SPIO@AuNS. The mean residence time (MRT) was 204.3 ± 19.4 (min), and mean systemic clearance (CL) was 23.1 ± 6.7 (%ID/g blood).

Table 1 summarizes the biodistribution of ^{111}In-labeled, PEGylated SPIO@AuNS at 24 h after intravenous injection. Relatively high uptake in the liver, spleen, kidney, and lung was observed in mice, with or without exposure to an external magnetic field. However, no significant differences in the uptake of nanoparticles in these organs were noted between the magnet and no magnet groups. On the other hand, the tumor uptake of ^{111}In-labeled SPIO@AuNS increased significantly, from 1.22% ID/g tumor in the absence of the external magnet to 2.34% ID/g in the presence of the external magnet (p-*value* = 0.05) (Table 1).

DISCUSSION

This study demonstrates the multi-functionality of SPIO@AuNS. Our results show that SPIO@AuNS can be imaged with MRI, mediate heating through photothermal effect, and be directed into target areas in the presence of an external magnet.

Previous data on SPIO@AuNS showed a relaxivity (R_2) value of 369 $\text{mmol}^{-1}\text{s}^{-1}$ [27]. In the current study, this relaxivity value translated into a darkening of the agar phantom in T2-weighted MR imaging (Fig. 2) and a decrease in T2* values in tumors injected with SPIO@AuNS (Fig. 3). The high NIR absorbance in the region of 700–900 nm (Fig. 1C) also translated into a temperature increase upon irradiation with an NIR laser in agar gel containing SPIO@AuNS (Figure 2A & 2B) and in tumors receiving intratumoral injection of SPIO@AuNS (Fig. 4). Significantly, only in tumors injected with SPIO@AuNS was the temperature elevated above 54°C, a threshold temperature above which ablation of tumor cells is ensured after 1 second of laser exposure [31]. Pathological results confirm that the tumors treated with SPIO@AuNS and irradiated with the NIR laser had a significantly greater degree of necrosis than the tumors treated with saline plus NIR laser or the tumors treated with SPIO@AuNS alone (Fig. 5). Thus, SPIO@AuNS is an MRI-visible, efficient photothermal coupling agent.

In addition to its role in visualizing the intratumoral distribution of SPIO@AuNS, MRI was used to monitor the temperature change during PTA therapy. The temperature dependency on water chemical shift (α) does not change significantly as a function of tissue type for the

proton resonance frequency method of MRTI, and $\alpha = -0.0097$ ppm/°C is generally used for tissue studies [32, 33]. However, because of the presence of SPIO, we had to confirm that the relationship between the temperature change and the shift in proton resonance frequency remained the same in SPIO@AuNS before any *in vivo* experiments were done. Our results show that at a therapeutically relevant concentration (6.7×10^{11} NS/mL), there was no difference in the temperature sensitivity with or without SPIO@AuNS, indicating that SPIO is unlikely to affect temperature measured with MRTI (Fig. 2E & 2F). Data acquired both with an agar phantom and *in vivo* in tumors confirmed that simultaneous T2*-weighted MRI and MRTI was feasible using the same imaging protocol.

To further characterize the magnetic properties of SPIO@AuNS *in vivo*, the biodistribution of intravenously injected ^{111}In-labeled, PEGylated SPIO@AuNS in mice bearing A431 tumors was studied in the absence and presence of an external Nd-Fe-B magnet (pulling force = 1.6 lbs). The nanoparticles displayed relatively high uptake in the liver, spleen, kidney, and lung (Table 1). Pharmacokinetic data also showed that SPIO@AuNS had a relatively short blood half-life of 10.7 min and 163.7 min for $T_{1/2,\alpha}$ and $T_{1/2,\beta}$, respectively. These results suggest that even with PEG coating, the 90-nm SPIO@AuNS nanoparticles cannot evade the reticuloendothelial system. The relatively high uptake in the lung suggests that SPIO@AuNS formed larger aggregates upon injection into the blood, resulting in their being trapped in the lung. Thus, future studies are necessary to optimize the physiochemical properties of SPIO@AuNS in order to extend their blood half-life and improve their biodistribution pattern.

One of the major challenges for the *in vivo* application of gold-shelled magnetic nanostructures is the delivery of these nanoparticles. The efficacy of most of these systems is often compromised due to the presence of biological barriers, especially the reticuloendothelial system (RES) that efficiently remove nanoparticles from the blood. To increase effectiveness of gold-shelled magnetic nanostructures, their physiochemical properties have to be carefully controlled. These properties include size, shape, morphology, charge, and surface chemistry. Previously, several groups have attempted the synthesis of gold-shelled SPIO-containing magnetic nanostructures having plasmon absorption in the NIR region [34]. All of the these gold-shelled magnetic nanoparticles, with the exception of the yolk-shell-structured gold nanoparticles, had an average diameter of 200 nm or greater [35–39]. The SPIO@AuNS reported here had an average diameter of ~90 nm. As shown by Zhang et al. [30], reducing the size of SPIO@AuNS is an efficient way to influence the pharmacokinetics and biodistribution of gold nanoparticles, with smaller nanoparticles having a better chance of evading the reticuloendothelial system. Clearly, further reduction in the size of MRI-visible SPIO@AuNS (e.g., to ~40 nm) is desirable to achieve efficient targeting to solid tumors through the enhanced permeability and retention effect [13].

An increase of approximately 2-fold in the tumor uptake of PEGylated SPIO@AuNS was observed in mice that had a magnet applied to the surface of the skin at the tumors compared to the mice that did not have the magnet applied. This result suggests that the magnetism of the SPIO@AuNS allowed them to be directed to the tumors by means of an external magnetic field gradient.

This study was conducted as a proof-of-concept approach to demonstrate the efficacy for the potential use of SPIO@AuNS for real-time imaging and phothothermal ablation. Therefore, the experimental parameters, such as concentrations and laser power used were based upon previous experience and published data. Optimal treatment conditions, including the minimum nanoparticle concentration suitable for MRI visualization and external magnet-directed targeting, the lowest laser power and treatment time possible to induce sufficient cell killing etc., were not determined. Moreover, the accumulation and elimination

pathways, as well as possible toxicity must be evaluated before these nanoparticles are translated into the clinic.To the best of our knowledge, this is the first study to demonstrate PTA therapy with simultaneous T2*-MRI and MRTI for real-time monitoring *in vivo*. It is anticipated that SPIO@AuNS may also be able to generate heat under an alternating magnetic field and, therefore, may be useful for the treatment of deep tissues where NIR light cannot reach.

Acknowledgments

Supported in part by the National Institutes of Health (grant R01 CA119387), the John S. Dunn Foundation, Odyssey Fellowship (to M.P.M.), and SPORE Head and Neck Career Development Award P50CA097007 (to M.P.M.).

REFERENCES

1. Curley SA, Izzo F, Delrio P, Ellis LM, Granchi J, Vallone P, et al. Radiofrequency ablation of unresectable primary and metastatic hepatic malignancies: results in 123 patients. Ann Surg. 1999; 230:1–8. [PubMed: 10400029]
2. Fiedler VU, Schwarzmaier HJ, Eickmeyer F, Muller FP, Schoepp C, Verreet PR. Laser-induced interstitial thermotherapy of liver metastases in an interventional 0.5 Tesla MRI system: technique and first clinical experiences. J Magn Reson Imaging. 2001; 13:729–37. [PubMed: 11329194]
3. Liapi E, Geschwind J-FH. Transcatheter and ablative therapeutic approaches for solid malignancies. J Clin Oncol. 2007; 25:978–86. doi:10.1200/jco.2006.09.8657. [PubMed: 17350947]
4. Seki T, Wakabayashi M, Nakagawa T, Itho T, Shiro T, Kunieda K, et al. Ultrasonically guided percutaneous microwave coagulation therapy for small hepatocellular carcinoma. Cancer. 1994; 74:817–25. [PubMed: 8039109]
5. Vogl TJ, Straub R, Eichler K, Sollner O, Mack MG. Colorectal carcinoma metastases in liver: laser-induced interstitial thermotherapy--local tumor control rate and survival data. Radiology. 2004; 230:450–8. [PubMed: 14688400]
6. Brieger J, Pereira PL, Trubenbach J, Schenk M, Krober S-M, Schmidt D, et al. In vivo efficiency of four commercial monopolar radiofrequency ablation systems: A comparative experimental study in pig liver. Invest Radiol. 2003; 38:609–16. [PubMed: 14501488]
7. Solomon SB, Nicol TL, Chan DY, Fjield T, Fried N, Kavoussi LR. Histologic evolution of high-intensity focused ultrasound in rabbit muscle. Invest Radiol. 2003; 38:293–301. [PubMed: 12750619]
8. Hilger I, Hiergeist R, Hergt R, Winnefeld K, Schubert H, Kaiser WA. Thermal ablation of tumors using magnetic nanoparticles: An in vivo feasibility study. Invest Radiol. 2002; 37:580–6. [PubMed: 12352168]
9. Diederich CJ. Thermal ablation and high-temperature thermal therapy: overview of technology and clinical implementation. Int J Hyperthermia. 2005; 21:745–53. [PubMed: 16338857]
10. Frericks BB, Ritz P Jr, Albrecht T, Valdeig S, Schenk A, Wolf K Jr, et al. Influence of Intrahepatic Vessels on Volume and Shape of Percutaneous Thermal Ablation Zones: In Vivo Evaluation in a Porcine Model. Invest Radiol. 2008; 43:211–8. [PubMed: 18340244]
11. O'Neal DP, Hirsch LR, Halas NJ, Payne JD, West JL. Photo-thermal tumor ablation in mice using near infrared-absorbing nanoparticles. Cancer Lett. 2004; 209:171–6. [PubMed: 15159019]
12. Hirsch LR, Stafford RJ, Bankson JA, Sershen SR, Rivera B, Price RE, et al. Nanoshell-mediated near-infrared thermal therapy of tumors under magnetic resonance guidance. Proc Natl Acad Sci U S A. 2003; 100:13549–54. [PubMed: 14597719]
13. Lu W, Xiong C, Zhang G, Huang Q, Zhang R, Zhang JZ, et al. Targeted photothermal ablation of murine melanomas with melanocyte-stimulating hormone analog-conjugated hollow gold nanospheres. Clin Cancer Res. 2009; 15:876–86. [PubMed: 19188158]
14. Melancon MP, Lu W, Yang Z, Zhang R, Cheng Z, Elliot AM, et al. In vitro and in vivo targeting of hollow gold nanoshells directed at epidermal growth factor receptor for photothermal ablation therapy. Molecular cancer therapeutics. 2008; 7:1730–9. [PubMed: 18566244]

15. Weissleder R. A clearer vision for in vivo imaging. Nat Biotechnol. 2001; 19:316–7. [PubMed: 11283581]
16. Wang W, Ke S, Wu Q-P, Charnsangavej C, Gurfinkel M, Gelovani JG, et al. Near-infrared optical imaging of integrin avb3 in human tumor xenografts. Mol Imaging. 2004; 3:343–51. [PubMed: 15802051]
17. Loo C, Lowery A, Halas N, West J, Drezek R. Immunotargeted nanoshells for integrated cancer imaging and therapy. Nano Lett. 2005; 5:709–11. [PubMed: 15826113]
18. Huang X, El-Sayed IH, Qian W, El-Sayed MA. Cancer cell imaging and photothermal therapy in the near-infrared region by using gold nanorods. J Am Chem Soc. 2006; 128:2115–20. [PubMed: 16464114]
19. Kramer NA, Donker HC, Otto J, Hodenius M, Senegas J, Slabu I, et al. A concept for magnetic resonance visualization of surgical textile implants. Invest Radiol. 45:477–83. [PubMed: 20531013]
20. Yakar D, Hambrock T, Huisman H, Hulsbergen-van de Kaa CA, van Lin E, Vergunst H, et al. Feasibility of 3T dynamic contrast-enhanced magnetic resonance-guided biopsy in localizing local recurrence of prostate cancer after external beam radiation therapy. Invest Radiol. 45:121–5. [PubMed: 20065860]
21. Mack MG, Vogl TJ. MR-guided ablation of head and neck tumors. Magn Reson Imaging Clin N Am. 2002; 10:707–13. vi. [PubMed: 12685501]
22. Carter DL, MacFall JR, Clegg ST, Wan X, Prescott DM, Charles HC, et al. Magnetic resonance thermometry during hyperthermia for human high-grade sarcoma. Int J Radiat Oncol Biol Phys. 1998; 40:815–22. [PubMed: 9531365]
23. MacFall J, Prescott DM, Fullar E, Samulski TV. Temperature dependence of canine brain tissue diffusion coefficient measured in vivo with magnetic resonance echo-planar imaging. Int J Hyperthermia. 1995; 11:73–86. [PubMed: 7714372]
24. Bankson JA, Stafford RJ, Hazle JD. Partially parallel imaging with phase-sensitive data: Increased temporal resolution for magnetic resonance temperature imaging. Magn Reson Med. 2005; 53:658–65. [PubMed: 15723414]
25. Alexiou C, Schmid R, Jurgons R, Kremer M, Wanner G, Bergemann C, et al. Targeting cancer cells: magnetic nanoparticles as drug carriers. Eur Biophys J. 2006; 35:446–50. [PubMed: 16447039]
26. Chertok B, Moffat BA, David AE, Yu F, Bergemann C, Ross BD, et al. Iron oxide nanoparticles as a drug delivery vehicle for MRI monitored magnetic targeting of brain tumors. Biomaterials. 2008; 29:487–96. [PubMed: 17964647]
27. Ji X, Shao R, Elliott AM, Stafford RJ, Esparza-Coss E, Bankson JA, et al. Bifunctional Gold Nanoshells with a Superparamagnetic Iron Oxide-Silica Core Suitable for Both MR Imaging and Photothermal Therapy. J Phys Chem C. 2007; 111:6245–51.
28. Taylor BA, Hwang KP, Elliott AM, Shetty A, Hazle JD, Stafford RJ. Dynamic chemical shift imaging for image-guided thermal therapy: analysis of feasibility and potential. Medical physics. 2008; 35:793–803. [PubMed: 18383702]
29. Taylor BA, Hwang KP, Hazle JD, Stafford RJ. Autoregressive moving average modeling for spectral parameter estimation from a multigradient echo chemical shift acquisition. Medical physics. 2009; 36:753–64. [PubMed: 19378736]
30. Zhang G, Yang Z, Lu W, Zhang R, Huang Q, Tian M, et al. Influence of anchoring ligands and particle size on the colloidal stability and in vivo biodistribution of polyethylene glycol-coated gold nanoparticles in tumor-xenografted mice. Biomaterials. 2009; 30:1928–36. [PubMed: 19131103]
31. Welch A. The thermal response of laser irradiated tissue. IEEE JQE. 1984; 20:1471–81.
32. Senneville D, Quesson B, Moonen CTW. Magnetic resonance temperature imaging. Int J Hyperthermia. 2005; 21:515–31. [PubMed: 16147437]
33. McDannold N. Quantitative MRI-based temperature mapping based on the proton resonant frequency shift: review of validation studies. Int J Hyperthermia. 2005; 21:533–46. [PubMed: 16147438]

34. Melancon M, Lu W, Li C. Gold-shelled magneto/optical nanostructures: Challenges for in vivo applications. Mat Res Soc Bull. 2009; 34:415–21.

35. Kim J, Park S, Ji EL, Jin SM, Lee JH, Lee IS, et al. Designed fabrication of multifunctional magnetic gold nanoshells and their application to magnetic resonance imaging and photothermal therapy. Angew Chem Int Ed. 2006; 45:7754–8.

36. Stoeva SI, Huo F, Lee JS, Mirkin CA. Three-layer composite magnetic nanoparticle probes for DNA. J Am Chem Soc. 2005; 127:15362–3. [PubMed: 16262387]

37. Salgueirino-Maceira V, Correa-Duarte MA, Farle M, Lopez-Quintela A, Sieradzki K, Diaz R. Bifunctional gold-coated magnetic silica spheres. Chem Mater. 2006; 18:2701–6.

38. Chen M, Kim YN, Lee HM, Li C, Cho SO. Multifunctional magnetic silver nanoshells with sandwichlike nanostructures. J Phys Chem C. 2008; 112:8870–4.

39. Lim IS, Njoki PN, Park H-Y, Wang X, Wang L, Mott D, et al. Gold and magnetic oxide/gold core/shell nanoparticles as bio-functional nanoprobes. Nanotech. 2008; 19:1–11.

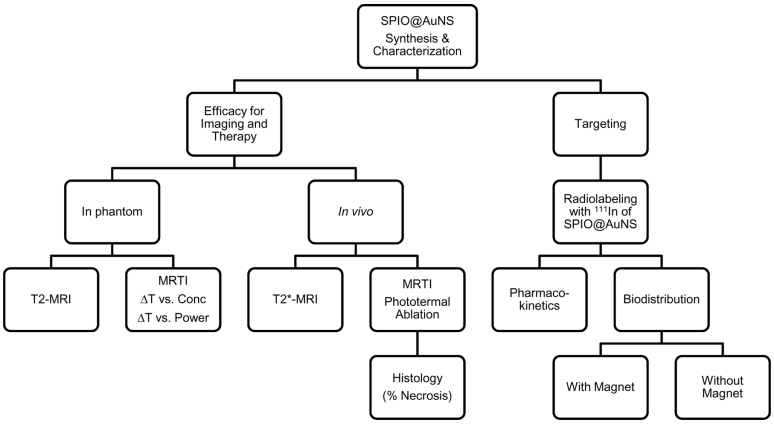

Fig. 1.
Experimental scheme.

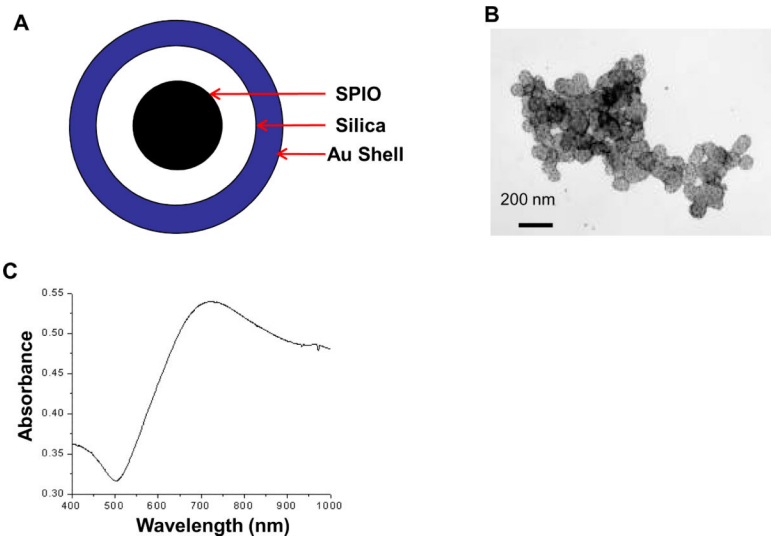

Fig. 2.

(A): Schematic representation of SPIO@AuNS. SPIO was coated with amorphous silica, which was then grown with a monolayer of gold on the shell. (B): A typical transmission electron microscope image of SPIO@AuNS. The particles had an average diameter of 90 nm. (C): Absorbance spectrum of SPIO@AuNS. Notice the high absorption at 650–900 nm, which is essential for photothermal ablation using a near-infrared laser.

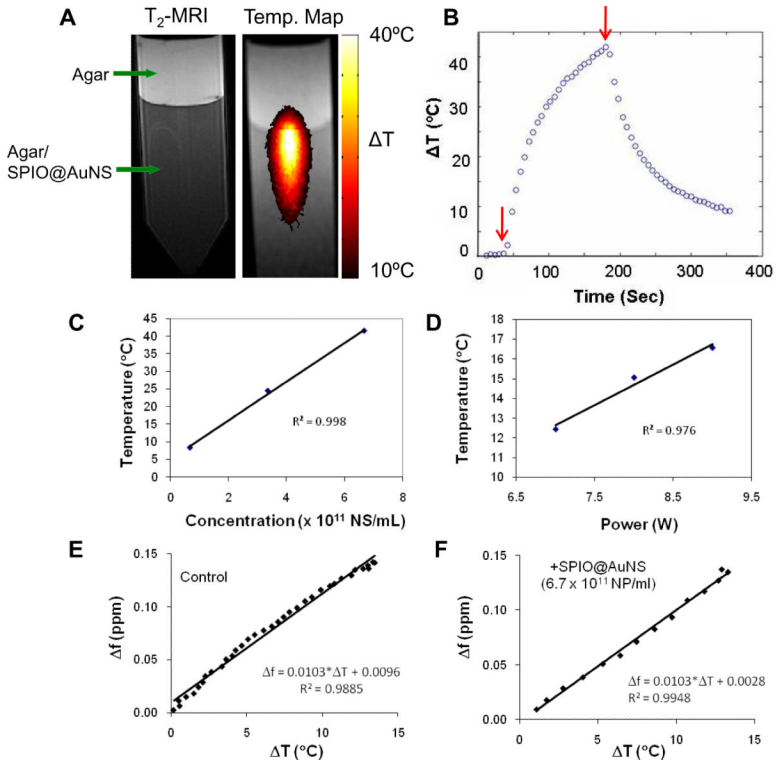

Fig. 3.

(A): T2-weighted magnetic resonance imaging (left) and magnetic resonance temperature imaging (right) of agar gel containing SPIO@AuNS covered with a layer of plain gel. The gel was irradiated with a near-infrared laser at 24 W/cm^2 for 3 min. (B–D): Plots of temperature as a function of time (B), as a function of nanoshell concentration (C), and as a function of laser power (D). Arrows in (B) indicate duration of laser irradiation. (E–F): Temperature sensitivity coefficients measured in agar phantoms using agar gel containing SPIO@AuNS at a concentration of 6.7×10^{11} NS/mL. The temperature sensitivity was calculated as the slope of the regression line for the frequency shift (Δf in ppm) versus temperature change (ΔT).

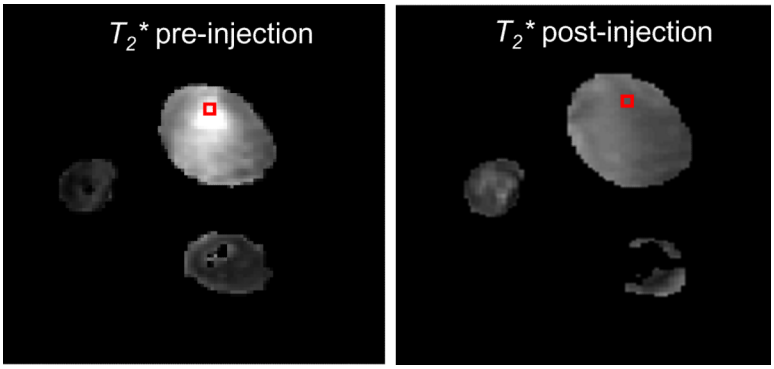

Fig. 4.

Representative T2*-weighted MR images of mice bearing A431 tumors before and after injection of the SPIO@AuNS. Notice the darkening of the tumor after the injection of SPIO@AuNS, which indicates a decrease in T2*.

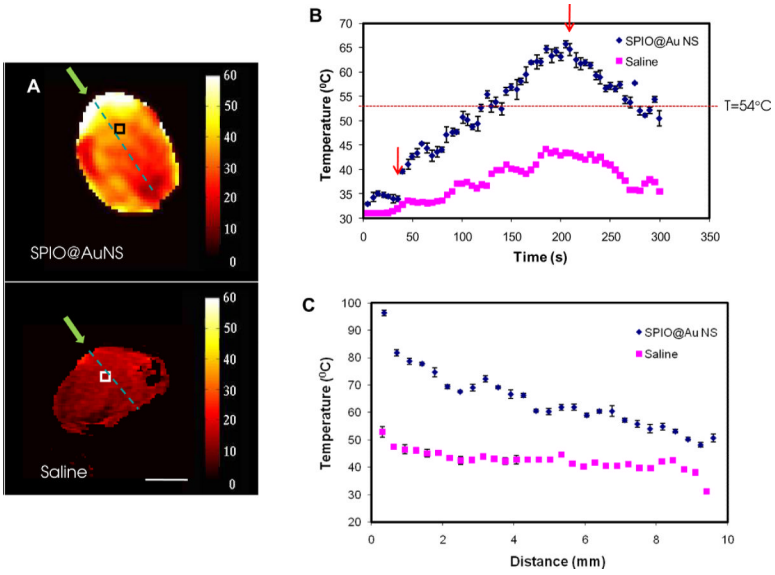

Fig. 5.

(A): *In vivo* magnetic resonance temperature imaging of a tumor injected intratumorally with SPIO@AuNS (top) and saline (bottom). Twenty-four hours after the injection of the agents, A431 tumors were irradiated with an 808-nm laser. Green arrows indicate the light path. Bar = 5 mm. (B) Plot of temperature elevation versus time, at 30 s before laser treatment, during laser treatment (180 s, 4 W/cm^2), and 90 s after laser treatment. Only in tumors injected with SPIO@AuNS was the temperature elevated above the 54° threshold (dotted line) to ensure irreversible thermal ablation of tumors cells. Square boxes in (A) indicate the treatment volumes from which the temperature versus time curves were plotted in (B). Arrows indicate the time points at which the laser was turned on and switched off. (C) Representative plot of temperature versus depth from the tumor surface.

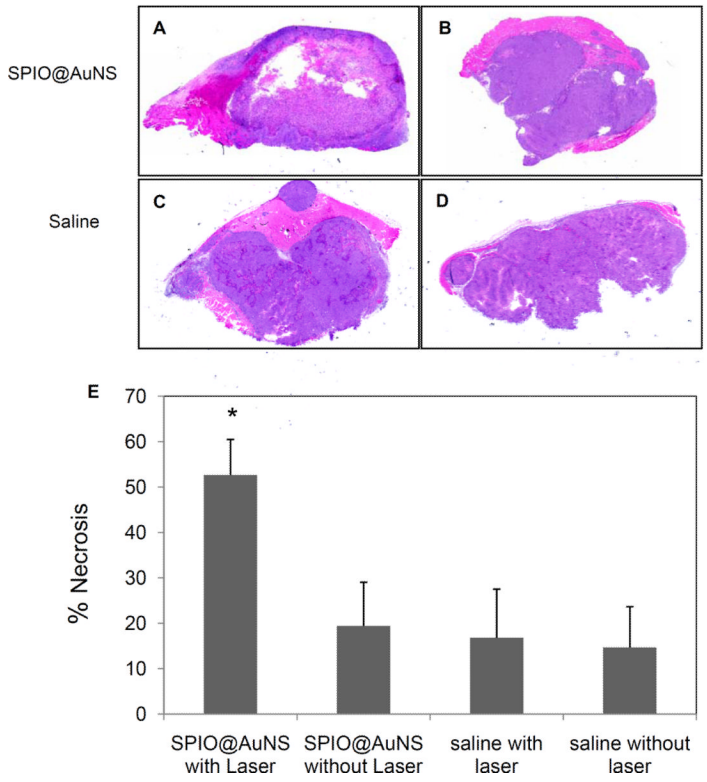

Fig. 6.

Representative hematoxylin and eosin–stained slides of the tumors excised 24 h after near-infrared (NIR) laser irradiation (A &C) and 48 h after intratumoral injection of SPIO@AuNS (A & B) or saline (C & D). The control groups were not treated with NIR laser (B & D). (E) Quantification of degree of necrosis. Percent necrosis is calculated by dividing the area of necrosis with the whole tumor multiplied by 100. Treatment with SPIO@AuNS and NIR laser (A) induced greater degree of necrosis compared with controls (B, C, and D). Asterisk (*) indicates p-value<0.01.

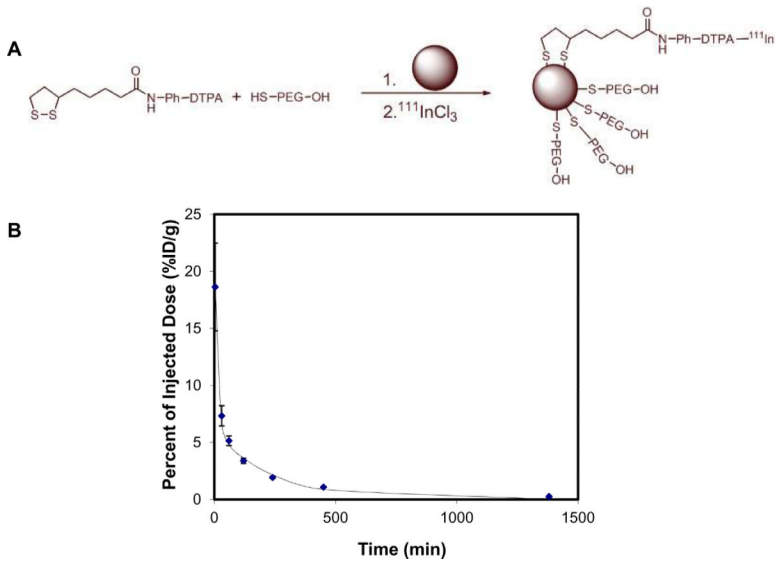

Fig. 7.

(A): Schema for the synthesis of ^{111}In-labeled SPIO@AuNS. (B): Blood activity-time profile of ^{111}In-labeled SPIO@AuNS (n =7).

Table 1

Biodistribution of ^{111}In-labled, PEGylated SPIO@AuNS in the presence and absence of an external magnet (% Injected dose/g of tissue).

	Blood	Heart	Liver	Spleen	Kidney	Lung	Muscle	Tumor
Magnet	0.79 ± 0.13	2.25 ± 0.82	107.6 ± 26.5	42.11 ± 9.17	28.02 ± 11.23	50.61 ± 26.23	0.38 ± 0.06	2.34 ± 0.73
No Magnet	0.69 ± 0.08	2.59 ± 1.00	76.94 ± 24.13	29.90 ± 6.07	28.86 ± 15.68	44.54 ± 16.65	0.31 ± 0.07	1.22 ± 0.05
p value	0.16	0.34	0.11	0.07	0.47	0.38	0.11	0.05